

# THE EMERGENT 1.1-1.7 MICRON SPECTRUM OF THE EXOPLANET COROT-2B AS MEASURED USING THE HUBBLE SPACE TELESCOPE

ASHLEE N. WILKINS<sup>1</sup>, DRAKE DEMING<sup>1</sup>, NIKKU MADHUSUDHAN<sup>2</sup>, ADAM BURROWS<sup>3</sup>, HEATHER KNUTSON<sup>4</sup>,  
PETER MCCULLOUGH<sup>5</sup> & SUKRIT RANJAN<sup>6</sup>

*Draft for the Astrophysical Journal*

## ABSTRACT

We have used Hubble/WFC3 and the G141 grism to measure the secondary eclipse of the transiting very hot Jupiter CoRoT-2b in the 1.1-1.7  $\mu\text{m}$  spectral region. We find an eclipse depth averaged over this band equal to  $395^{+69}_{-45}$  parts per million, equivalent to a blackbody temperature of  $1788 \pm 18\text{K}$ . We study and characterize several WFC3 instrumental effects, especially the “hook” phenomenon described by Deming et al. (2013). We use data from several transiting exoplanet systems to find a quantitative relation between the amplitude of the hook and the exposure level of a given pixel. Although the uncertainties in this relation are too large to allow us to develop an empirical correction for our data, our study provides a useful guide for optimizing exposure levels in future WFC3 observations. We derive the planet’s spectrum using a differential method. The planet-to-star contrast increases to longer wavelength within the WFC3 bandpass, but without water absorption or emission to a  $3\sigma$  limit of 85 ppm. The slope of the WFC3 spectrum is significantly less than the slope of the best-fit blackbody. We compare all existing eclipse data for this planet to a blackbody spectrum, and to spectra from both solar abundance and carbon-rich (C/O=1) models. A blackbody spectrum is an acceptable fit to the full dataset. Extra continuous opacity due to clouds or haze, and flattened temperature profiles, are strong candidates to produce quasi-blackbody spectra, and to account for the amplitude of the optical eclipses. Our results show ambiguous evidence for a temperature inversion in this planet.

*Subject headings:* stars: individual (CoRoT-2) – planets and satellites: individual (CoRoT-2b) – planets and satellites: atmospheres – techniques: photometric – techniques: spectroscopic

## 1. INTRODUCTION

Very Hot Jupiters are gas-giant exoplanets with orbital periods less than about 3 days. The close proximity of VHJs to their host stars enhances the influence of irradiation, tidal forces, and stellar activity on their structure and evolution. CoRoT-2b (Alonso et al. 2008) is a VHJ of particular interest because of lingering questions about the structure of its atmosphere, which can be studied with observations of its secondary eclipse. Alonso et al. (2009) announced the first secondary eclipse observations of CoRoT-2 in the *CoRoT* optical waveband, followed by the mid-infrared *Spitzer* secondary eclipse measurements of Gillon et al. (2010), re-analyzed and expanded with Warm *Spitzer* eclipses by Deming et al. (2011). Alonso et al. (2010) added a secondary eclipse point in the  $K_s$  band. The analysis of Gillon et al. (2010) favored a poor day-night-side heat distribution in CoRoT-2b’s atmosphere. Deming et al. (2011) found a high 4.5  $\mu\text{m}$  flux as the only disagreement

with a solar-composition, equilibrium chemistry model of the atmospheric temperature structure. Deming et al. (2011) considered possible emission in the 4.5  $\mu\text{m}$  band from CO mass loss. Both works question, but do not rule out, the presence of a temperature inversion in the atmosphere caused by an upper atmosphere absorber. Madhusudhan (2012) finds that either a carbon-rich or solar abundance non-inverted model fits the data available in the literature.

These widely varied, competing explanations for this planet demonstrate the importance of spectroscopic observations. CoRoT-2b clearly does not fit the standard solar-composition, equilibrium chemistry model that satisfactorily describes many planets in its class, and we explore the anomalous spectral shape. For a clear illustration of CoRoT-2b’s standing as an outlier among VHJs, see Knutson et al. (2010). CoRoT-2 is a very active star, a young Solar analog, and yet a temperature inversion cannot be ruled out and the planet does not fit clearly into the otherwise well-defined inverted/non-inverted planet classifications. This curious state of the planet is perhaps due to a magnetic interaction between the planet (Lanza et al. 2009) and CoRoT-2. Any further understanding would require more measurements of the planet in new wave bands.

In this paper, we use the G141 infrared grism on the Hubble Space Telescope’s Wide-Field Camera 3 (HST’s WFC3) to detect the day-side thermal emission spectrum of CoRoT-2b from 1.1  $\mu\text{m}$  to 1.7  $\mu\text{m}$ . The CoRoT-2 system is part of an HST Cycle-18 program that ob-

<sup>1</sup> Department of Astronomy, University of Maryland, College Park, MD 20742 (USA); awilkins@astro.umd.edu

<sup>2</sup> Institute of Astronomy, University of Cambridge, Cambridge CB3 0HA (GB)

<sup>3</sup> Department of Astrophysical Sciences, Princeton University, Princeton, NJ 08544-1001 (USA)

<sup>4</sup> Division of Geological and Planetary Sciences, California Institute of Technology, Pasadena, CA 91125 (USA)

<sup>5</sup> Space Telescope Science Institute, Baltimore MD 21218 (USA)

<sup>6</sup> Harvard-Smithsonian Center for Astrophysics, Cambridge, MA 02138 (USA)

**Table 1**  
CoRoT-2 Observation Summary

Visit	UT Date & Time (hr:min-hr:min)	Number of Exposures	Orientation Angle
A	10-18-2010 11:12-16:45	271	80.4°
B	9-16-2011 09:37-15:07	276	93.9°
C	9-23-2011 07:41-13:11	275	90.7°

served a wide range of HJs/VHJs in transit and secondary eclipse, and gives us the basis for new insights into the instrumental effects of WFC3 (Deming et al. 2013; Huitson et al. 2013; Line et al. 2013; Mandell et al. 2013; Ranjan et al. 2013, submitted). In what follows, we describe the observations of the CoRoT-2 system in §2 and the initial stages of data analysis in §3. In §4 we place our observations in the larger context of other HST programs with WFC3 in order to provide a comprehensive systematic description of the instrumental effects encountered in these observations. We then present our methods of obtaining the band-integrated secondary eclipse curve (§5) and derivation of the spectrum (§6) of CoRoT-2b. Finally, we use our results to constrain models for the atmosphere of the planet in §7, and we summarize in §8.

## 2. OBSERVATIONS

We observed CoRoT-2 using the G141 grism of WFC3 (1.1-1.7  $\mu\text{m}$ ), in three separate visits, each comprising four orbits of HST and hereafter called visits A, B, and C. We used the 128 $\times$ 128-pixel subarray of the 1024 $\times$ 1024-pixel detector. At the beginning of each visit, we acquired a single direct image of the system with the F139M filter, a medium-band filter centered at 1.39  $\mu\text{m}$ ; the location of the target in this direct image defines the initial wavelength solution for the grism spectra. A summary of the observations is in Table 1.

Most of our observations in program 12181, including those of CoRoT-2, were executed before the advent of spatial scan mode (McCullough & MacKenty 2012). Lacking the spatial scan, WFC3 observations of relatively bright stars can be inefficient, because the time required to transfer the data greatly exceeds the exposure time for bright exoplanet host stars. We maximize the efficiency by using subarrays and by exposing the detector to fluence levels approaching or equaling saturation. Even at a saturated exposure level, an unsaturated signal is available because the detector is sampled ‘up the ramp’ multiple times within each exposure, and all the samples are saved in the data. Isolating less than the full number of samples, a linear signal can be obtained even in the saturated case. Our CoRoT-2 grism data are exposed so that the brightest pixel contains about 70,000 electrons in a full exposure, which is approximately the level of 5% non-linearity.

## 3. INITIAL DATA ANALYSIS

In order to explore whether our results are sensitive to details of the data analysis, we use two parallel but independent methods to process the data. To avoid confusion with the visit terminology (A, B, C), we denote the two methods as  $\alpha$  and  $\beta$ . Method  $\alpha$  makes more explicit corrections and manipulations of the data than does method  $\beta$ . Exoplanet signals are subtle, and the more the data

are processed, the more the potential for adding numerical noise that may mask the small exoplanet signal or even fooling oneself into detecting a false signal. Our dual-track analysis allows us to evaluate the trade-off between the most ‘complete’ method versus the potential for degrading the results by over-processing of the data. It also allows us to evaluate what corrections are necessary, and what corrections can be neglected. Upon measurement of the eclipse curve, the methods yield consistent results.

Method  $\alpha$  uses “flt” FITS image files retrieved from the Mikulski Archive at Space Telescope (MAST) server, located at the Space Telescope Science Institute (STScI). The “flt” files were calibrated through the WFC3 pipeline’s high-level task, calwf3, which includes two low-level tasks, wf3ir and wf3rej, that apply to the infrared channel. wf3ir performs standard calibrations, including corrections for bias, non-linearity, dark current, and bad pixels due to energetic particle hits, while wf3rej completes more bad pixel rejection and combines images. Rajan (2010) gives details of this pipeline. We multiply the resultant signal rates (electrons per second) by the integration time to infer the accumulated signal on each pixel, in electrons.

Method  $\beta$  begins with “ima” FITS files from the MAST server. These files give the ‘sample-up-the-ramp’ values of each pixel at 4 times during each 22-second exposure, and are processed to correct for non-linearity, but not to reject energetic particle hits. We process these files (minimally) by fitting a linear slope to the four samples as a function of time for each pixel, to determine the rate at which electrons are accumulating in the pixel. Our linear fit weights each sample of a given pixel by the square-root of the signal level, as appropriate for Poisson errors. Multiplying the fitted slope by the 22-second integration time yields the accumulated signal in electrons. This process does not include any correction for energetic particle hits. Rather, we correct those at later stages of the  $\beta$ -analysis, and we also evaluate the success of the non-linearity corrections by repeating the  $\beta$ -analysis and restricting the linear fit versus sample time to only the first three samples.

Using the smaller subarray means the grism data consists of the central 128 pixel columns of the first-order spectrum out of the 150 on a larger (sub)array. Nevertheless, using the 128 subarray increased the efficiency of the observations (i.e., minimizing data transfer time on the spacecraft), more than justifying the loss of points at the edges of the grism response.

To extract the spectrum of the star+planet system, we sum the pixels after background subtraction, using a box defining a range in rows. We adopt a box size of height 61 pixels (a central pixel, plus 30 above and below it). The box length is the full 128 pixel length of the subarray, but we later trim the spectrum in wavelength.

We sum the box over rows to produce spectra, and we further sum over wavelength to produce a ‘white light’ photometric time series. The spectra are very stable in position (jitter less than several hundredths of a pixel), and the intensity level falls by 2.5 orders of magnitude over the 30-pixel half-height of the box. Therefore we use fixed integral coordinates for the box in each visit, and we weight each pixel equally when performing the sum. This spectral extraction is the same for both the  $\alpha$  and  $\beta$  analyses.

In the following, we discuss the various sub-elements of the data analysis (§3.1,3.2) including the wavelength calibration (§3.3) and flat-fielding (flux calibration, §3.4), while the more extensive task of characterizing the instrumental systematics is discussed in §4.

### 3.1. Bad Pixel Correction

Bad pixel correction due to energetic particle hits is part of the calwf3 processing used for our  $\alpha$  analysis. Additional pixels not identified by calwf3 may still be erroneously high or low in value and need correction. For both  $\alpha$  and  $\beta$  analyses, we identify and correct bad pixels immediately prior to the spectral extraction (i.e., before summing the box). Our  $\alpha$  analysis inspects pixels in each column of the spectral box (i.e., a single wavelength) that deviate significantly from a Gaussian profile of the spectral trace. Such deviations are virtually always characterized by much higher intensity levels. Those pixels that are more than 10 times greater than the fitted Gaussian value are replaced by a 7-pixel median in the vertical direction (perpendicular to the dispersion) at that wavelength.

Our  $\beta$  analysis must be more sophisticated as regards bad pixels, since these data have not been processed by calwf3. We examine the ratio of a given pixel to the total of all pixels in that row, i.e., the ratio of a single pixel to the sum over wavelength at each spatial position. Because of spatial pointing jitter, pixel intensities can vary with time in an absolute sense, but their relative variation should be similar at all wavelengths. We examine the ratio as a function of time (i.e., for each exposure) and we identify instances where a given pixel does not scale with its row sum. We identify  $> 4\sigma$  outliers, and correct them using a 5-frame median value of the ratio at that time.

### 3.2. Background Subtraction

For both the  $\alpha$  and  $\beta$  analyses, we calculate the background individually for each exposure by using pixels outside of the spectral box. Specifically, the pixels used are those that lie directly below the spectrum on the subarray, which is the section of the subarray corresponding to the width of the spectrum and extending from the bottom edge of the spectral box to the bottom edge of the subarray. We construct a histogram of intensity values in these pixels and fit a Gaussian to the histogram. The adopted background value is the intensity corresponding to the central value of the fitted Gaussian, and we do assume that it is independent of wavelength to the limit of our precision. This is typically a few tens of electrons per pixel, several orders of magnitude less than the signal in the stellar spectrum, and the sum is thus also significantly lower when calculating the white light curve and

its corresponding background. Background subtraction therefore has a relatively minor effect on our analysis.

### 3.3. Wavelength Calibration

Wavelength calibration utilizes both the direct image and the spectral image, as the wavelength of a given pixel depends upon its location on the detector relative to the direct image. Kuntschner et al. (2009) outline the procedure for wavelength calibration in an STScI calibration report. The equations governing the wavelength for a pixel at a given x-position in the first-order spectrum are:

$$\lambda(x) = dldp_0 + dldp_1 \Delta x \quad (1)$$

where

$$\begin{aligned} dldp_0 &= a_0^0 + a_0^1 x_{center} \\ dldp_1 &= a_1^0 + a_1^1 x_{center} + a_1^2 y_{center} + a_1^3 x_{center}^2 + \\ & a_1^4 x_{center} y_{center} + a_1^5 y_{center}^2 \\ \Delta x &= x - x_{center} \end{aligned}$$

The terms  $x_{center}$  and  $y_{center}$  are the central coordinates of the direct image. The coefficients ( $a_0^0$ ,  $a_0^1$ , etc.) are calculated in Kuntschner et al. (2009).

In performing this calibration, we found that the calibrated grism response (sensitivity) curve did not line up precisely in wavelength space with the observed response (see Figure 1). We therefore adjusted the coefficients empirically to obtain optimal agreement with the observed grism response curve and with the wavelengths of two stellar hydrogen lines (Pa- $\beta$  at  $1.282 \mu\text{m}$  and Br-12 at  $1.646 \mu\text{m}$ ). These adjustments yielded:

$$\begin{aligned} a_0^0 &\rightarrow 0.997 \times a_0^0 \\ a_0^1 &\rightarrow 0.90 \times a_0^1 \\ a_1^0 &\rightarrow 1.029 \times a_1^0 \end{aligned}$$

We used these adjusted values in the calibration presented in this work and also successfully applied them to other data sets in this HST program. Therefore, this empirical correction is not specific to this target or these visits, and we in fact used another object in the program (TrES-2) to find the correction, as it was observed on the larger subarray and thus the observations include all 150 pixels of the spectrum.

### 3.4. Flux Calibration

The flat field and sensitivity curve of the G141 grism on the WFC3 detector are the two components of flux calibration, and both are wavelength-dependent.

For imaging observations, calwf3 applies the flat field to the data, but flat-fielding of grism data must be done by the observer. STScI provides a flat-field cube for the G141 grism. This cube is a four-extension FITS file, and each extension is the size of the full WFC3 IR array. For a given pixel on the data image with a given wavelength, the flat-field value for that pixel is given by a polynomial function with coefficients defined by the values of the flat-field cube extensions at the pixel’s location.

This method is described in the aXe handbook (Kümmel et al. 2011) and laid out with the equations

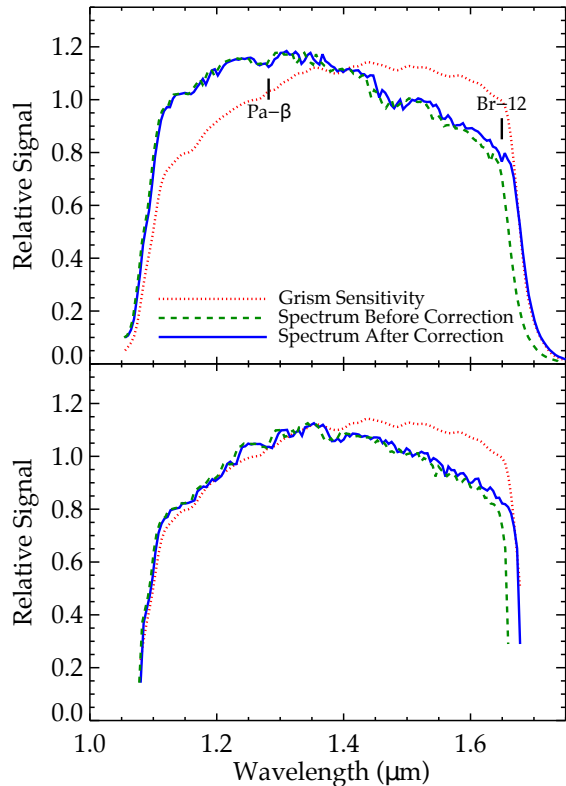


**Figure 1.** Flat-field-corrected spectrum of TRES-2 (*above*) and CoRoT-2 (*below*). Each plot shows the WFC3 G141 grism sensitivity curve (*red, dotted line*) and the spectrum before (*green, dashed line*) and after (*blue, solid line*) the correction has been made to the wavelength solution coefficients. The two hydrogen lines, Pa- $\beta$  (1.282  $\mu\text{m}$ ) and Br-12 (1.646  $\mu\text{m}$ ), the two lines in TRES-2 used to adjust the wavelength coefficients, are also marked here. To get a normalized spectrum, one must simply divide by the sensitivity curve.

that follow. For a pixel at position  $(i,j)$ , they define a normalized wavelength coordinate,  $x$ :

$$x = \frac{\lambda - \lambda_{min}}{\lambda_{max} - \lambda_{min}}$$

The parameters  $\lambda_{min}$  and  $\lambda_{max}$  are constants found in the flat-field cube header. The flat field value of a pixel  $(i,j)$  with normalized wavelength coordinate  $x$  is then a polynomial function in  $x$ :

$$f(i, j, x) = a_0 + a_1x + a_2x^2 + a_3x^3 \quad (2)$$

where  $a_0$ ,  $a_1$ ,  $a_2$ , and  $a_3$  are the values at  $(i,j)$  in the zeroth, first, second, and third extension arrays in the flat-field cube file, respectively. For both our  $\alpha$  and  $\beta$  analyses, we apply the flat-field correction to the spectral box by dividing by the corresponding flat-field “box,” generated pixel-by-pixel from the method above.

STScI also provides the wavelength-dependent sensitivity of the G141 grism. In Figure 1, we plot the scaled sensitivity curve over a flat-fielded spectrum from a single exposure of TRES-2, along with the two hydrogen lines used as reference points in adjusting the wavelength calibration coefficients.

### 3.5. Second, Overlapping Source

CoRoT-2 has a companion star, so our analysis must remove or correct for this second source. The direct image of CoRoT-2 appears in Figure 2, where the second, fainter source is evident. The proximity of the second source in the image depends on the orientation angle of the telescope, and varies between the three visits, but it is close enough to be of concern for source contamination. The spectra overlap minimally in visits A and C, but there is significant overlap in visit B, which has the lowest orientation angle and thus the smallest distance between the two spectra of the three observations. The orientation angles, which only vary a few degrees from each other, are reported in Table 1.

#### 3.5.1. Characterization

This second source is an infrared source, 2MASS J19270636+0122577, but is just barely spatially resolved by the 2MASS observations. In the planet’s discovery paper, Alonso et al. (2008) suggest it may be a late-K or M-type star, and Schröter et al. (2011) identify it as a late K-type star. Both works posit that it may be gravitationally bound to CoRoT-2. We here address how to remove, or correct the effect, of this second source from the flux of the CoRoT-2 system. We have explored two approaches. Our  $\alpha$  analysis removes the second source prior to extracting the grism spectrum from the 2-D frames. Our  $\beta$  analysis includes the second source in the extracted grism spectra, and corrects the derived exoplanetary spectrum after deriving that stellar spectrum.

The location of the second source allows us to generate its spectrum, albeit in a limited wavelength range. Its spatial offset results in losing the long-wavelength end of its spectrum. Comparing the partial spectrum to a grid of Kurucz models shows general agreement with the findings of Schröter et al. (2011); a temperature of 4000 K and surface gravity  $\log(g) = 4.0$ , produces the best agreement with the observed partial spectrum. That corresponds to a late K- or early M-type main sequence star.

#### 3.5.2. Removal

In our  $\alpha$  analysis, the strategy for removing the second source from visits A and C is to determine the average spatial shape of the source’s signal, and scale and subtract it from each column of the spectral box. We fit a Gaussian plus a second-order polynomial baseline to the spatial profile at each column of the data. Averaging that fit over all exposures then approximates the signal from the second source for a given column, after scaling the average to represent the amplitude of the second source for each column. The original spectral trace – the plot of wavelength-integrated flux versus spatial pixel – appears in Figure 2, as well as the corrected spectral trace (overplotted), showing significant improvement.

For visit B, the task is more difficult. The peaks of the two sources are separated by just four pixels, compared to twelve and ten pixels for visits A and C, respectively. The overlap leaves too few points to use a fitting procedure to isolate and approximate the source. Instead, we use the descent of the PSF on the opposite side of CoRoT-2 from the overlap of the second source, and mirror the PSF column-by-column onto the side with overlap. We subtract the mirrored PSF, and fit a Gaussian column-by-column to the difference. Averaging that fit

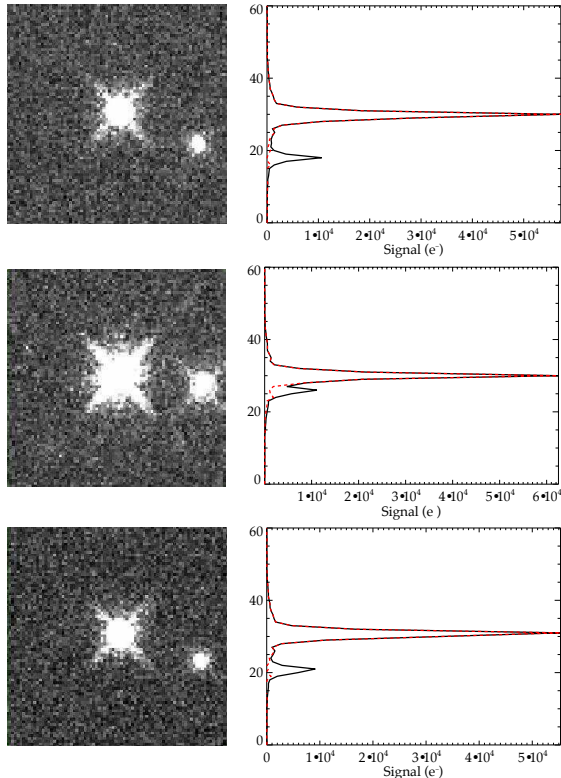


**Figure 2.** *Left:* The direct image of CoRoT-2 (brightest object, center of each image) and the infrared source nearby in visits A (*top*), B (*middle*), and C (*bottom*). *Right:* A vertical profile of the first-order spectrum resulting from a horizontal dispersion of the light to the right of the direct image for each of the three visits; the solid, black line is the original trace, while the dashed, red line is the trace after correction. The variation in degree of overlap of the spectral trace is due to variation in the orientation angle of the telescope between the visits, which changes the proximity of the second source’s spectrum to that of the target. The orientation angle was limited to the range  $76^\circ < \text{ORIENT} < 166^\circ$  by telescope operation parameters, and the actual angles were  $93.9^\circ$ ,  $80.4^\circ$ , and  $90.7^\circ$ , for visits A, B, and C.

over all exposures, we approximate and remove the second source from each column for visit B.

#### 4. SYSTEMATICS: CHARACTERIZATION

Our data exhibit trends in the measured stellar intensity that are not manifestations of physical stellar or planetary phenomena. Instead, they represent tendencies of the detector to report signal counts that are different from what actually fell on a given pixel.

We note that instrument-related systematic errors in WFC3 exoplanetary spectroscopy are believed to be less severe than in NICMOS observations (Gibson et al. 2011; Crouzet et al. 2012; Deming et al. 2013; Swain et al. 2013). Nevertheless, instrument effects do exist in the WFC3 data, especially for observations taken before the advent of spatial scan mode (McCullough & MacKenty 2012) such as ours. Some aspects of these instrumental effects were discussed by Swain et al. (2013). Berta et al. (2012) reached nearly the photon limit in their analysis of WFC3 G141 transit spectra of the super-Earth GJ1214b, as did Deming et al. (2013) for two giant transiting exoplanets with the implementation of the spatial scan mode. We will discuss the analysis of the Berta et al. (2012) work and how we

modified it for more general purposes in §5.

We identify three primary manifestations of systematic error, and all are patterns in intensity as a function of time. The first is a continuous trend of the source’s white light curve lasting the entire length of a visit, during which the intensity gradually decreases with time (or increases, in one case). This “visit-long ramp” is linear in nature (to within the errors), and continuous between orbits. Its slope varies widely between observations, not only among the CoRoT-2 visits, but among all in our HST program. Its strict linearity and variation even when separately observing the same star places it clearly in the category of instrumental effects rather than stellar modulations, but the exact cause is an open question. The second systematic error feature is a decrease of intensity as a function of time, which repeats for every orbit. This effect is apparent in the pixels *not* illuminated by the source spectrum – including the pixels we use for the background subtraction – and is shown for the examples of CoRoT-2 and others in Figure 3. For most objects in the program, the effect shows a smooth, exponential decrease in the signal for these pixels over the course of an orbit, though some observations show an effect in more of an “S”-shape instead. Removal of the background, as per the method described in 3.2, removes any discernible presence of this effect, which allows us to conclude first that the effect is isolated to the lowest-valued pixels, and second that we need not perform further tasks to eliminate this orbit-long feature, as the problem is solved by careful background definition and subtraction. We find no definitive cause, though we suspect it may be due to scattered light from the Earth’s limb.

The third example of systematic error is an increase in intensity of the source’s white light curve which occurs on a shorter time scale, over the course of several exposures, and which repeats three or more times in every orbit. We call this the “hook” (Deming et al. 2013) because of its characteristic shape, which is a steep jump for the first one to three exposures and then a flattening<sup>7</sup>. The hook appears to a varying degree in all of the observations, and produces a significant distortion in the data. Examples of the hook within a single orbit of observations for four different objects are shown in Figure 4. The reset of this pattern corresponds with the time when the data stored in the WFC3 buffer are sent to the solid-state recorder on the spacecraft. This causes a short break in observations, and also resets the detector. Neither of the other two primary systematic effects appear to have any dependence on times of data transfer.

The hook pattern is of similar shape in all sets of observations in the program, but the parameters of its manifestation, e.g., length of time, number of exposures, number of iterations, vary from object to object. Figure 4 shows examples of the pattern in four different objects; the shape of the pattern is similar, but the amplitude of the hook and the time between buffer dumps (and thus the number of exposures and total time of each hook) varies. Swain et al. (2013) concluded that it was most significant for the  $512 \times 512$  subarray. We concur that it is often prominent at  $512 \times 512$ , and it is considerably

<sup>7</sup> Some investigators call this effect a ‘ramp’, but we advocate different terminology so as not to confuse it with the visit-long ramp, and also to distinguish it from the Spitzer ramp.

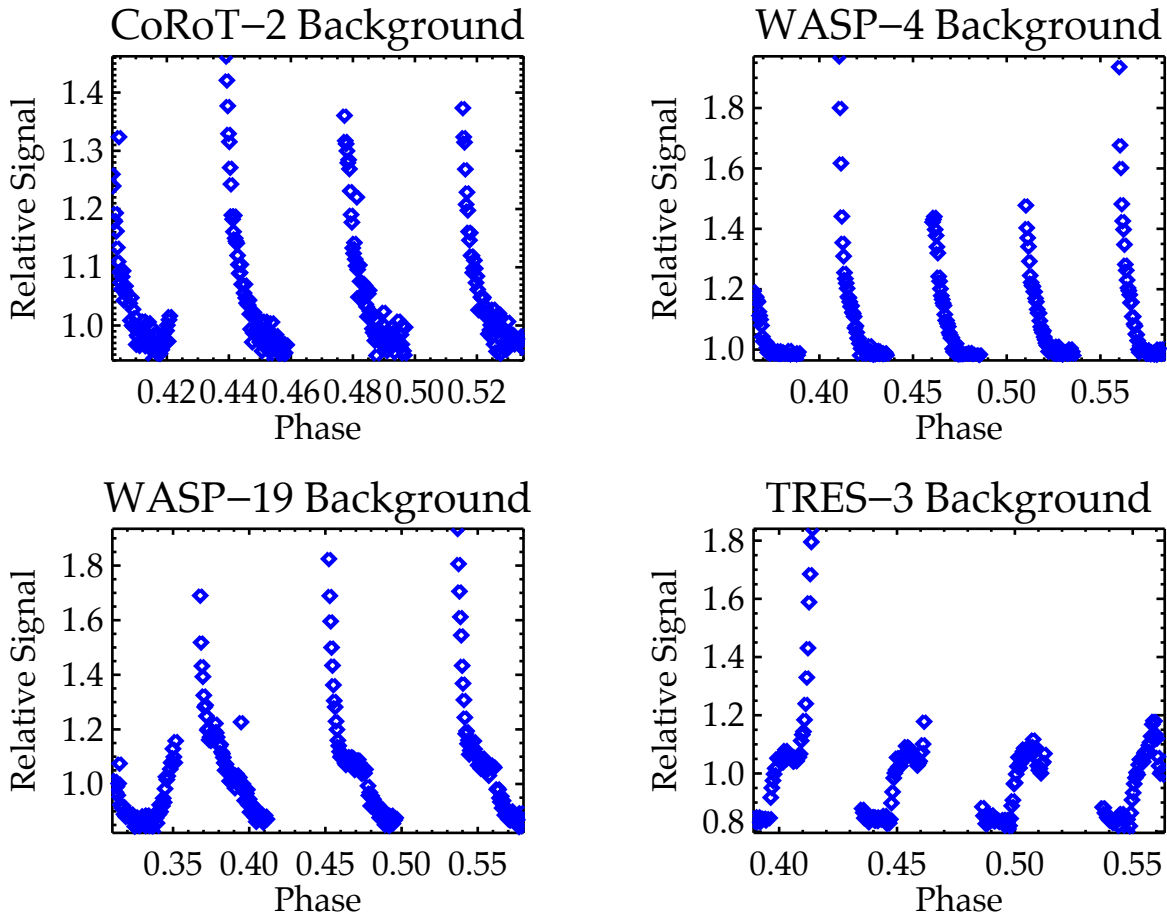


**Figure 3.** The normalized signal measured from the background pixels over the course of the observations. This systematic effect resets after each orbit of the telescope (between orbits there is a gap in time as HST passes behind the Earth). For most objects in our program, the effect is a smooth exponential decrease, as shown here for CoRoT-2 and WASP-4 in the upper panels. For some observations the shape is different, an irregular "S"-shape, as for WASP-19 and TRES-3 in the lower panels.

steeper for longer-duration patterns on  $512 \times 512$ , but we detect it in other subarrays also. The prominence of the pattern correlates with brightness of the star.

While the visit-long slope appears to be linear, both the orbit-long and hook effects are exponential in shape, and therefore each begins as a very strong effect and then becomes nearly indiscernible in the final exposures of each hook pattern.

There are further apparent systematic effects seen in the first orbit of every observation; they are most likely due to telescope settling and readjusting to a new pointing, and do not have a consistent pattern. Therefore we discard the first orbit once we begin applying corrections to the systematic effects for the purpose of calculating the wavelength-integrated transit depth, and the spectrum of the planet. Since the eclipse of CoRoT-2b is covered by three visits, loss of the first orbit is only a minor perturbation for our analysis.

#### 4.1. Persistence Correction

One potential cause of the hook effect is detector persistence, the phenomenon in which trapped charge in an exposure is slowly released in following exposure(s) to produce a falsely increased signal detection (Smith et al. 2008). STScI publishes persistence models and even predictions of persistence for a given exposure based on the

exposures prior to it. The predictions are for an additive effect, and the data product for a given exposure is an image array the size of the original exposure, but with each pixel value equal to the the predicted persistence, so the correction is simply to subtract the corresponding pixel values. The persistence is low for the first exposure, but jumps up quickly and remains at a higher value until the time of the data transfer, when it, too, resets. The additive correction as given by STScI do decrease the severity of the hook, but they do *not* entirely remove the hook, and we conclude that the hook is a combination of a additive and *multiplicative* effect. This will justify our methods of correction outlined and examined in the sections that follow. We have made the STScI persistence correction in our  $\alpha$  analysis. Our  $\beta$  analysis ignores additive persistence, as do most WFC3 exoplanetary investigations published to date.

#### 4.2. Pixel-by-Pixel Evaluation of the Hook

Berta et al. (2012) demonstrated that the hook is more prominent at high exposure levels. We have investigated the amplitude of the hook as a function of the per-pixel exposure level, and other parameters, and we seek quantitative relationships. For each pixel, we average the change in signal level over the multiple iterations of the pattern within one orbit, and then examine the change

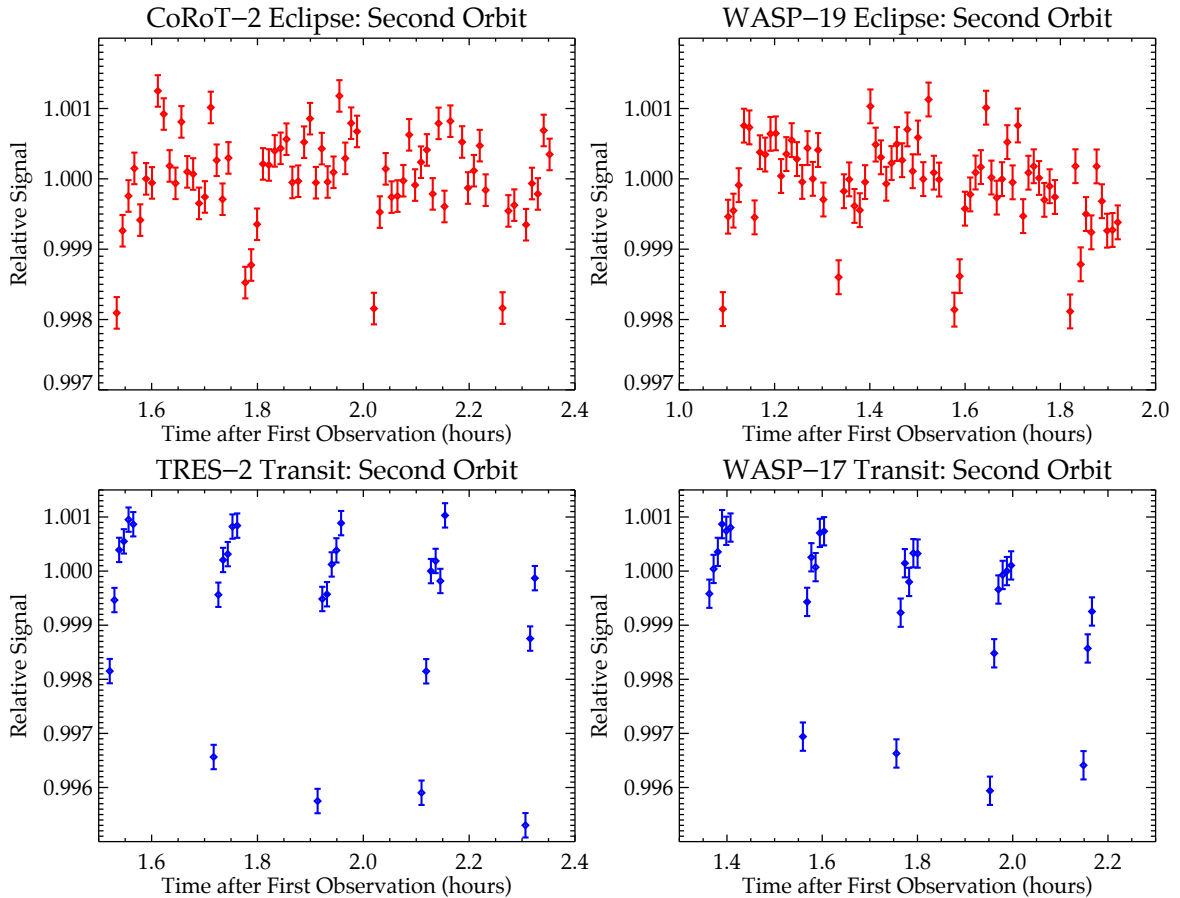


**Figure 4.** Four examples of the systematic hook pattern. WASP-19 and CoRoT-2 (*top*) were both observed on the smaller subarray, and have more exposures in the pattern, a more subtle pattern, and less time in between iterations. HAT-7 and TRES-2 (*bottom*) were both observed on the larger subarray, and have fewer exposures in the pattern, a more obvious pattern, and a much larger gap in time between the observations.

as a function of time within the pattern, flux of the pixel, and location of the pixel on the detector.

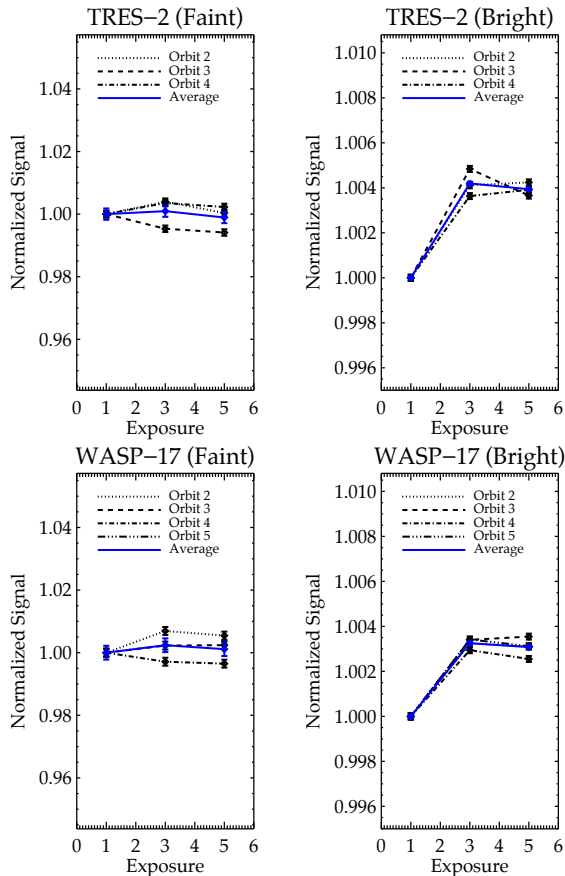
The average shape of the hook for two objects in the program can be seen in Figure 5. The normalized signal is shown against the exposure number within the pattern. For each visit, the pixels have been split between those with flux below the mean and those with flux above the mean. This is done to confirm that the existence of the hook does indeed depend upon the flux of the pixel.

Figure 6 shows this dependence of the additive change on the flux of the pixels, where every pixel has been plotted by its initial flux and “jump” in electrons between the first exposure and the last exposure in the pattern. The jump is statistically insignificant below a certain original pixel value, but shows a reliable parabolic rise starting around 30,000 electrons. The scatter is nevertheless remarkably large, which ultimately means that we cannot depend on a unique quantitative relation to correct this effect.

In principle, the hook could be removed by using Figure 6 to predict the magnitude of the jump for a pixel given its initial flux in the first exposure of the pattern, and thereby correct each pixel in each image. We attempted such a correction, and it does remove the ob-

vious appearance of the hook pattern, but it leaves the data with much more scatter than is acceptable, due to the wide variations seen in Figure 6.

We also examined the amplitude of the hook as a function of position on the detector. We find no correlation in column (wavelength) space, but some correlation with the slope of the hook pattern and the row on the detector, i.e., how far a given row is from the spatial center of the spectrum. This correlation does seem to strongly depend on which subarray we used. Especially in the case of the  $128 \times 128$  subarray, the slope of the trend is more positive for the rows of pixels below the central peak of the spectrum (in the direction perpendicular to dispersion), while the slope is less positive for those rows above the central peak. This correlation is weaker for the  $512 \times 512$  subarray, but still discernible. Figure 7 shows the correlation for the smaller subarray by demonstrating the shift in the spatial center of the spectrum between the starting and ending frames of the hook. Our finding that the nature of the hook depends on the row of the spectrum may be a significant clue to the nature of this effect. Reading the detector involves addressing the pixels by row, and it is conceivable that the hook is related to the manner in which the detector is addressed and



**Figure 5.** Examining the average shape of the hook pattern for two sets of observations. We calculated the total flux in the spectral box at the beginning, middle, and end of the pattern, averaged over all the iterations within an orbit, and then plotted the average normalized to the first average value. For each object shown, the pixels in the spectral box have been split in half about the median value: the faint half and the bright half, and then plotted separately. As is apparent with this split, the fainter pixels are not affected by whatever causes the pattern, while the brighter half are.

sampled. We conclude that the effect in Figure 7 cannot be explained by anything like telescope drift. The trend featured in Figure 7 is correlated with the hook and therefore the transfer of the detector buffer, a task performed with no relation to telescope motion.

## 5. WHITE-LIGHT ECLIPSE CURVE

We wish to produce a time series of the wavelength-integrated (‘white light’) signal measured from CoRoT-2 in order to determine the amplitude and central phase of the secondary eclipse. This will yield the total signal from the planet over the G141 bandpass, while the spectrum that we calculate in Sec. 6 will distribute that signal as a function of wavelength. We begin with the light curves for the three visits shown in Figure 8, then we correct these light curves to remove the instrumental systematic effects, and we combine the three visits to form a single eclipse curve as a function of orbital phase.

Berta et al. (2012) successfully removed systematic effects from their dataset. The steps of their **divide-oot** method for correcting a transit/eclipse curve are as follows, assuming a five-orbit set of observations, with orbits three and four in transit:

1. Ensure that all orbits have the same num-

ber of exposures. The fifth orbit usually has fewer exposures than orbits two, three, and four, so simply repeat the last element to make up the difference. Since the hook pattern is flatter at its end, this is a reasonable approximation.

2. Create an average out-of-transit orbit by simply averaging orbits two and five.
3. Divide each orbit (two, three, four, and five) by the average orbit.
4. Remove the artificial elements that were added in the first step.
5. Fit a line to the second and fifth orbits, as there is still usually a hint of the visit-long ramp. Divide by the linear fit to normalize the data in units of the stellar flux.

This method should yield an acceptable eclipse curve with out-of-transit flux normalized to unity. Application of **divide-oot** to objects in our HST program 12181 proved successful only in some cases (Ranjan et al. 2013, submitted). A modification of the method will be explained below.

### 5.1. Modified **divide-oot**

We observe CoRoT-2 in four orbits per visit, but each visit contains at most one orbit that is completely in-eclipse (when the planet does not contribute), and each visit contains the virtually unusable first orbit. For this reason and due to our significantly lower signal-to-noise ratio than for the Berta et al. (2012) planet’s observations – the GJ1214b transit depth is two orders of magnitude larger than the depth of the CoRoT-2b secondary eclipse in the same waveband and on the same grism – our CoRoT-2 data are not well-suited for the **divide-oot** method *per se*. Another issue with CoRoT-2 is the severity of the visit-long ramp, which causes trouble when trying to average pattern shapes before removing the ramp. Therefore, instead of dividing by an average *orbit*, we elect to divide by an average *pattern*, defined both by the occurrence of a buffer dump and through visual assessment, and we proceed as follows:

1. Identify the patterns that are out-of-eclipse. Divide the entire white-light curve by the median of the out-of-eclipse exposures from a single, early orbit (usually orbit 2). This normalizes the curve to unity.
2. Fit a line to the out-of-eclipse patterns, but exclude all points below intensity level 0.997. These outliers are due to the hook effect, and would bias the visit-long slope correction.
3. Divide by the fitted curve to re-normalize to unity.
4. Create an average pattern by averaging the out-of-eclipse patterns.
5. Divide each occurrence of the pattern in the entire white-light curve by the average pattern.

This creates a vast improvement in the data, with a significant reduction in the presence of systematic effects. We are also able to utilize the later patterns of the first



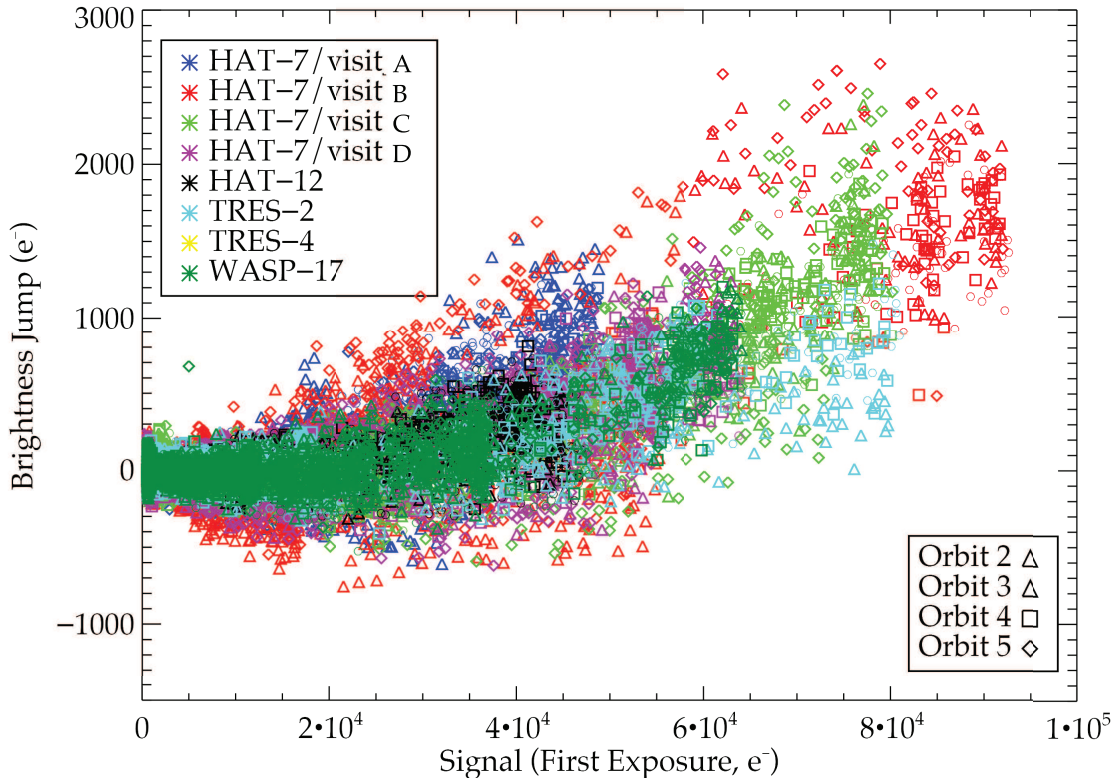


**Figure 6.** A quantification of an additive effect from the detector for a selection of objects. The hook pattern repeats multiple times in each orbit, and each visit has 4-5 orbits. For every orbit in every visit, coded by symbol and color, we have averaged the increase in measured flux from the first to the second-to-last exposure in each pattern for each pixel in the spectral box. This is plotted against the initial flux of each pixel in the first exposure of a hook. The increase is clearly dependent upon the flux level, and does not become apparent (on average) until a signal of about 30,000 electrons. The legend shows which visit corresponds to which color. The relation between initial flux and flux jump appears to be steeper for longer pattern times.

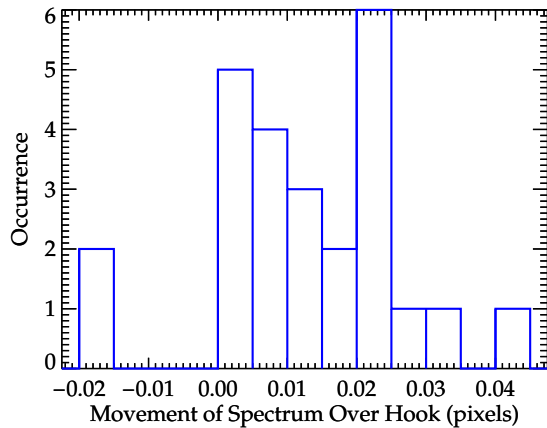


**Figure 7.** To measure any possible dependence of the hook effect on pixel row, we compared a Gaussian fit to the spectrum between the first and last observations of the hook for all iterations in the objects observed on the  $128 \times 128$  subarray. We show here that the location of the maximum point of the spectrum (the peak of the Gaussian) typically moves, and typically moves in the same direction, over the course of the hook. This indicates that the hook pattern has a row dependence.

orbit, rather than discarding it completely, as the problems presented by settling or other effects of unknown origin diminish significantly after one to two iterations of the pattern. An average pattern is plotted in the inset of Figure 8, and the corrected data are shown in com-

parison to our best-fit eclipse curve in Figure 9.

### 5.2. White-Light Eclipse Amplitude

With the corrected data in hand after applying our modified **divide-out** procedure, we fit an eclipse curve using the data from our  $\alpha$  analysis. We calculate the shape of the theoretical eclipse curve using expressions from Mandel & Agol (2002), with orbital parameters from Alonso et al. (2009), except for the orbital period where we adopt the updated value from Sada et al. (2012). In fitting the data, we vary only the central phase and amplitude of the eclipse, the latter by scaling the amplitude of the theoretical curve. We perform the fit using two  $\chi^2$ -minimization methods. First, we implement a Levenberg-Marquardt algorithm to vary the eclipse amplitude and central phase simultaneously, to find the global minimum in  $\chi^2$ . Second, we vary the central phase incrementally from 0.49 to 0.51 in steps of  $10^{-5}$ . At each step, we calculate the best-fit eclipse amplitude at that phase in closed form, using linear least-squares. Cycling through the range of trial central phases, we again find the global minimum  $\chi^2$ . Results from the two methods were in excellent agreement.

We find a best-fit eclipse depth of  $395_{-45}^{+69}$  ppm (parts per million); the fit is shown in Figure 9. The reduced  $\chi^2_{red} = 6.60$ ; as it was calculated estimating the error to be Poissonian, the ideal scenario, this  $\chi^2_{red}$  value indicates that the achieved per-point scatter is 2.6 times the photon noise. The error level, and the appearance of Fig-

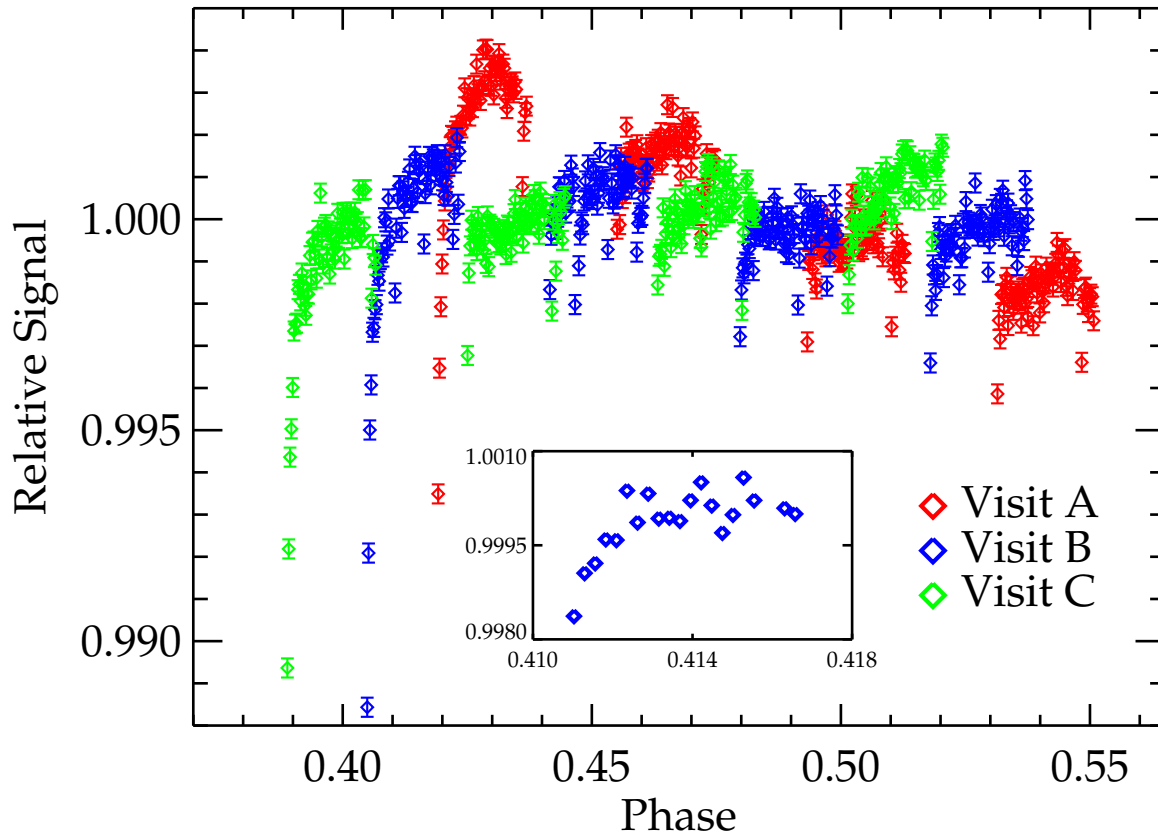


**Figure 8.** Phase plot of the wavelength-integrated flux from the three visits of CoRoT-2 before any corrections to the systematics have been applied. Visits A, B, and C are shown in red, blue, and green, respectively. *Inset:* An example of an “average pattern,” of the characteristic hook shape, corresponding to visit 23 and calculated by the modified **divide-oot** method described in §5.1. This pattern is calculated after removal of the linear visit-long ramp.

ure 9, suggests that red noise remains in the data, in spite of our modified **divide-oot** procedure. To verify the presence of red noise, we binned the residuals from the best-fit eclipse over  $N$  points per bin, and calculated the standard deviation of the binned points,  $\sigma_N$ . We solve for the slope of the relation between  $\log(N)$  and  $\log(\sigma_N)$  using linear least-squares. Poisson noise will produce a slope of  $-0.5$ , whereas we find a slope of  $-0.33 \pm 0.03$  for the Figure 9 data, confirming the presence of red noise.

Given the presence of red noise in the white light eclipse data, we assign errors to the best-fit eclipse parameters (eclipse amplitude and central phase) using the residual permutation (“prayer-bead”) method (Bouchy et al. 2005; Gillon et al. 2007). Figure 10 shows histograms of the results for the best-fit amplitude and central phase, based on the residual permutation fits. For reference, we fit Gaussians to these histograms. A Gaussian is a reasonable approximation to the central phase histogram, but the eclipse amplitude histogram has a higher central peak, and lower wings, than does a Gaussian. Our adopted errors are equivalent to the  $\pm 1\sigma$  points in the histograms, in the sense that 15.8% of the histogram area lies beyond each quoted  $1\sigma$  value (31.6% considering both ends of the range).

### 5.3. Eclipse Central Phase

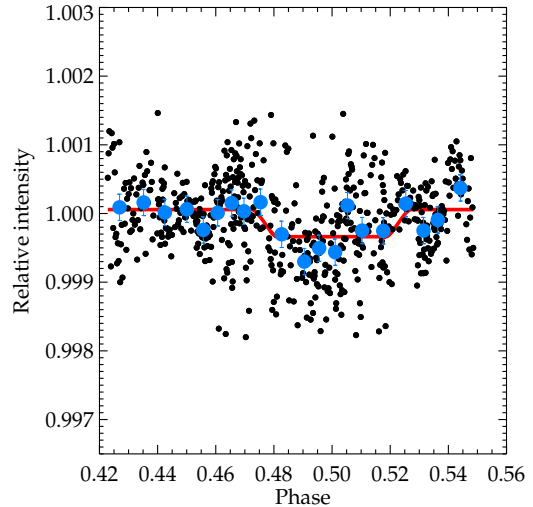


**Figure 9.** Wavelength-integrated light curve of CoRoT-2 after correction of the hook and visit-long ramps as described in section §5.1. The best-fit secondary eclipse curve is overplotted in red. The large points in blue represent averages over bins of 0.0063 in phase, about 15 minutes in time. The fit was performed on the actual data (black points); the binned data are shown merely for reference.

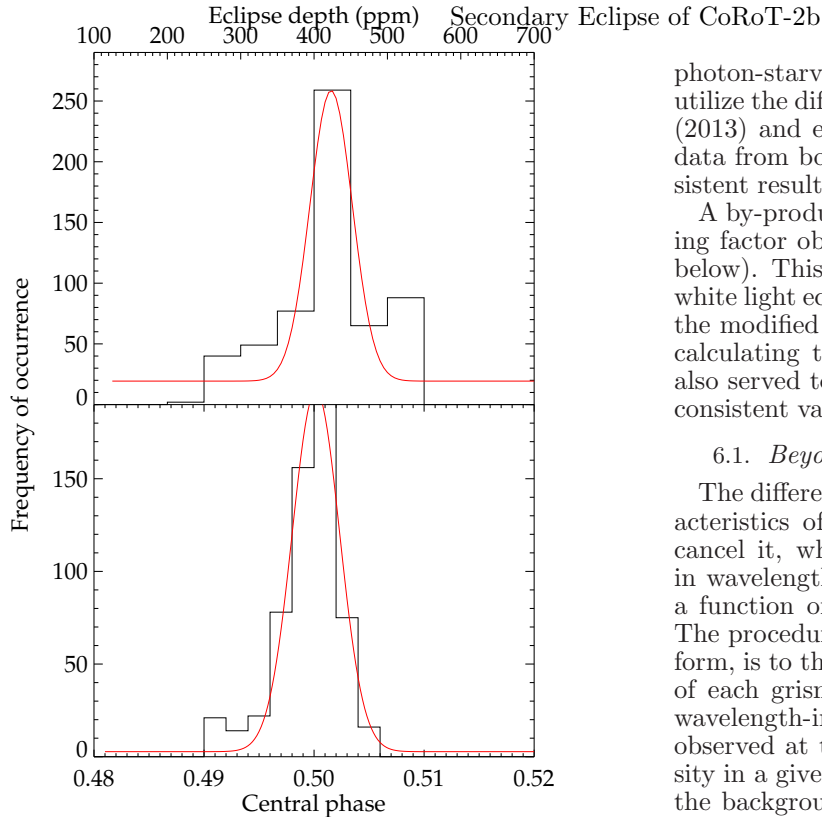


**Figure 10.** Error analysis for the amplitude and central phase of the white light eclipse. The frequency of occurrence is based on a total of 580 residual permutations. Upper panel: histogram of eclipse amplitudes in parts-per-million for the residual permutation error analysis of the eclipse amplitude. Lower panel: histogram from the residual permutation error analysis of the central phase of the eclipse.

Our best-fit eclipse is centered at a phase of  $0.4998 \pm 0.0030$ . The light-travel time across the orbit is 28 seconds. The central phase for a circular orbit would be 0.50019, consistent with our result, within our errors. Gillon et al. (2010) found the eclipse to occur slightly earlier than expected for a circular orbit, at phase  $0.4981 \pm 0.0004$ . (Deming et al. 2011) found a central phase of  $0.4994 \pm 0.0007$ , weakly supporting the result from Gillon et al. (2010). The low signal-to-noise – due to the shallower secondary eclipse at shorter wavelengths – of the eclipse in the WFC3 bandpass contributes to a relatively large error level for the central phase (approximately 4 to 8 times larger than the Spitzer errors). Although we find good agreement with a circular orbit, we cannot exclude the result of Gillon et al. (2010) who concluded that the orbit is slightly eccentric.

## 6. CALCULATION OF THE ECLIPSE SPECTRUM

Berta et al. (2012) used his **divide-oot** method for GJ1214b to derive the depth of transit as a function of wavelength, i.e., the transmission spectrum. In principle that method is applicable to exoplanetary spectra at secondary eclipse, but we use an alternate technique. We have at most one in-eclipse reference orbit (when the planet does not contribute) per visit. Moreover, CoRoT-2 is a relatively faint star ( $V=12.6$ ,  $H=10.4$ ). In the faint-source limit, dividing single-wavelength data by a single reference orbit would increase the random noise in the quotient to an unacceptable degree, because we are

photon-starved. To obtain the spectrum of the planet, we utilize the differential method described by Deming et al. (2013) and explained below. We apply this method to data from both our  $\alpha$  and  $\beta$  data analyses, finding consistent results.

A by-product of this method is a time-dependent scaling factor obtained by fitting a template spectrum (see below). This scaling factor is an excellent proxy for the white light eclipse, and we find consistent results between the modified **divide-oot** and differential methods when calculating that white light eclipse. That comparison also served to verify that our  $\alpha$  and  $\beta$  analyses produce consistent values for the white light eclipse depth.

### 6.1. Beyond **divide-oot**: the Differential Method

The differential method is intended to exploit the characteristics of the systematic hook pattern in order to cancel it, while also correcting for the effects of jitter in wavelength over time. The amplitude of the hook is a function of the flux level in the affected pixels (§4). The procedure of the differential method, in its simplest form, is to therefore extract the intensity in each column of each grism image, and divide that intensity by the wavelength-integrated intensity in the entire spectrum observed at that time. In other words, ratio the intensity in a given column on the detector (after subtracting the background, and integrating over rows) to the sum of all columns, and we repeat this process for the grism image at each orbital phase  $\phi$ . This ratio adds minimal noise, because the precision of the wavelength-integrated spectrum is much better than the precision of a single wavelength. Moreover, the ratio should be effective in removing the hook, as long as the wavelength used in the numerator is not too close to the edges of the grism response, where the intensity rolls-off to much smaller values, as does the hook (§4). The observed grism spectral intensity varies only modestly (Figure 1) over the 1.1-1.7  $\mu\text{m}$  range of our analysis. Thus, dividing a single wavelength by the sum of all wavelengths is a comparison of similar intensity levels, so we expect much of the hook pattern to cancel, and this expectation is met by the actual data (see below).

The differential method also removes the white-light eclipse. Specifically, the eclipse shown on Figure 9, by summing over wavelengths, will identically cancel. However, wavelength-to-wavelength *variations* in the eclipse depth will be preserved. We call these differences *differential depths* and we derive them either positive or negative, by fitting to the wavelength-ratioed data. We then add the depth of the white-light eclipse, reconstructing the full emergent spectrum of the planet at eclipse.

In actual practice, the implementation of this differential method is more complex than the simple division implied above. We do not explicitly divide by a wavelength integral; we use an equivalent but more subtle procedure that we now describe.

We must account for possible wavelength shifts in each grism spectrum. Wavelength shifts have two effects. First, a shift of the spectrum changes the intensity in a given column because the grism response varies with wavelength. Second, a shift in the spectrum changes the range of wavelengths sampled by a given column of the detector. We find that the wavelength shifts are of order 0.02-pixels, and they vary within an orbit, but tend to

reset and exhibit a similar pattern in subsequent orbits. Given this magnitude of shifts, the second effect mentioned above - a perturbation to the wavelength assigned to a given column - has negligible effect. We therefore ignore the wavelength perturbations per se, and we use the wavelength scale from the calibration described in §3.3. However, the first effect (changes in grism response with wavelength) is important, and we deal with it as follows:

1. For each visit, form a “template” spectrum of the star alone by summing the in-eclipse (planet hidden) spectra. Denote this spectrum by  $S_x$ , where  $x$  is the column coordinate on the detector.
2. Fit the template to each individual spectrum by re-sampling, shifting (in steps of  $10^{-4}$  pixels), and scaling  $S_x$  in intensity using linear least-squares. Perform this least-squares fit over a large range of shift values ( $\pm 0.1$ -pixels) and choose the shift that exhibits the best fit as judged by the standard deviation of the ratio.
3. Each individual spectrum,  $P_x$  at orbital phase  $\phi$ , matches a version of  $S_x$  with a scaling factor  $a$ :  $aS'_x + b$ . The prime marks the change in intensity due to the shift in  $x$ , and the zero-point constant  $b$  is negligibly small.
4. Form the ratio  $R_x^\phi = \frac{P_x}{aS'_x + b}$ .

An example of this basic process of shifting and fitting the template spectrum, for a randomly selected spectrum in visit C, is illustrated in Figure 11. However, our actual analysis adds an additional step in order to deal with the undersampling of the stellar spectrum as discussed by Deming et al. (2013). Between steps 3 and 4 above:

- 3.5. Smooth all of the spectra using a Gaussian kernel with FWHM = 4 pixels.

The choice of pixels (columns in wavelength) is dictated by the tradeoff between suppressing the undersampling, and preserving the spectral resolution.

The wavelength integrals of  $P_x$  and  $aS'_x + b$  are closely equal because of the fitting process that matches them. Moreover, the shape of  $S_x$  is constant over a visit, i.e., its value at any single wavelength, relative to its wavelength integral, is constant. Hence the point-by-point division described above is conceptually equivalent to dividing a single wavelength (equivalently,  $x$ -value) in  $P_x$  by the wavelength integral of  $P_x$ . However, our procedure has the advantage that we do not have to re-sample any spectra wherein the potential signal is present, or where the reference stellar spectrum is changing. Hence we introduce no extra noise in this process, while also correcting for wavelength jitter in the spectrum.

#### 6.1.1. The Spectrum of CoRoT-2b Using the Differential Method

Performing the procedure described above yields a set of ratio values  $R_x^\phi$  for each visit. We now combine visits as follows:

1. For each column of the detector  $x$ , fit a straight line to the  $R_x^\phi$ , where the inde-

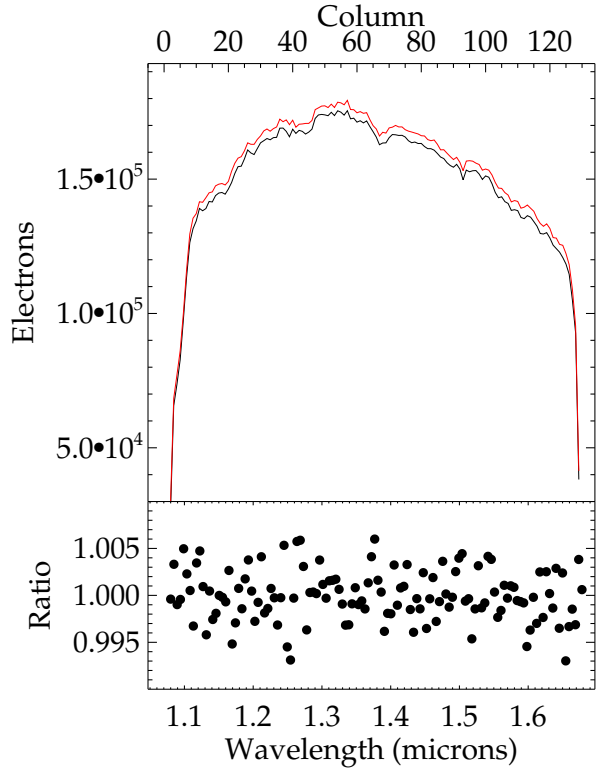


**Figure 11.** Top panel: Spectrum of the star + planet (black line) at a randomly selected time during visit A, compared with a best-fitting ‘star only’ spectrum (red line) constructed as an average of all of the in-eclipse spectra during visit A. (These spectra are prior to the smoothing that we employ.) The star-only spectrum was shifted in wavelength and scaled in intensity to provide the best fit to the star+planet spectrum (see text, however for this figure an additional 2% shift in intensity was added so that the two lines do not overlap). Bottom panel: ratio of the star+planet spectrum to the shifted and scaled star-only spectrum. The scatter (0.00245) is dominated by the photon noise of the spectrum in the numerator of the ratio.

pendent variable in the linear fit is phase  $\phi$ , and then divide by that line.

Dividing each visit by the linear fit removes any slight slopes that are present in each visit (as described by Berta et al. 2012 and §4) and places all three visits on a common scale.

2. Fit an eclipse curve to the combined  $R_x^\phi$  at each  $x$ , holding the central phase fixed at 0.5 for the eclipse fit, solving only for the depth.
3. Use the wavelength calibration to associate a wavelength with each column  $x$ ;  $R_x^\phi$  becomes  $R_\lambda^\phi$ .

The wavelength scale is sufficiently similar for each of the visits that we associate visit-averaged wavelengths with each  $x$ . The upper panel of Figure 12 shows the result of fitting an eclipse curve to the visit-combined  $R_\lambda^\phi$  at a randomly-selected wavelength. Because the white-light eclipse has been removed by the process used to generate the  $R_\lambda^\phi$ , the differential eclipse depth at individual wavelengths can be either positive or negative depending

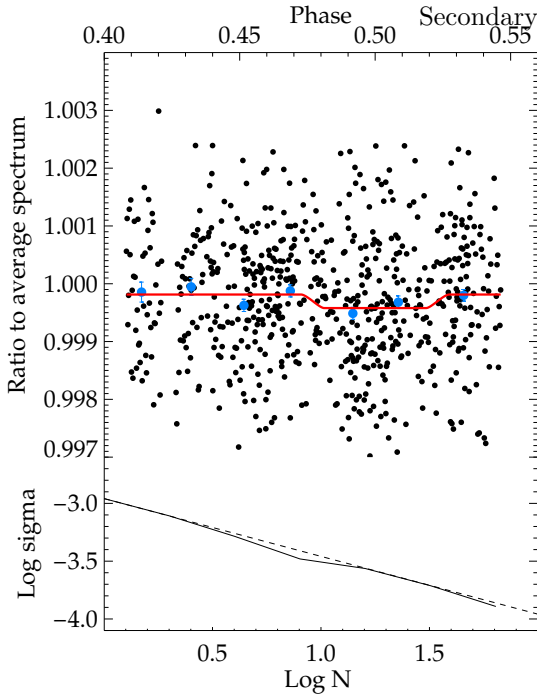


**Figure 12.** Top panel: Differential eclipse at a single randomly-selected wavelength ( $\lambda = 1.551 \mu\text{m}$ ). Bottom panel: Log of the observed dispersion (solid line) for bins of  $N$  points, versus  $\log N$ . The dashed line shows the relation expected for an inverse square-root dependence, as per photon noise.

on whether the intensity of the exoplanetary spectrum is greater or less at that wavelength compared to the average over the band defined by the grism response. Note that the scatter in the individual points on Figure 12 is large compared to these differential eclipse depths. However, the precision of the differential eclipse depths is much better than the single-point scatter in  $R_{\lambda}^{\phi}$ , and we also average adjacent wavelengths to derive spectral structure in the exoplanetary spectrum (see below).

As the final step,

4. We add the white-light eclipse depth (0.000495, §5.2) to the differential eclipse depths, and thereby derive the planet-to-star contrast versus wavelength.

This emergent spectrum of the planet is illustrated on Figure 13, from both our  $\alpha$ - and  $\beta$ -analyses. The upper panel shows the values for individual wavelengths, i.e., single columns of the detector, and the lower panel bins the results in bins of width  $0.05 \mu\text{m}$  (4 columns).

### 6.1.2. Errors

We have estimated the errors on the differential eclipse depths using two methods. For both methods, we remove the fitted differential eclipse and examine the properties of the point-to-point scatter (Figure 12, top) for each wavelength. First, we bin these points using bin widths of 2, 4, 8, 16, 32 and 64 points, and we calculate the scatter in those binned values. For Poisson noise, we expect that the scatter as a function of bin size  $\sigma(N)$  will decrease as  $N^{-0.5}$ . An example of the measured relation at a single randomly-chosen wavelength is shown in the lower panel of Figure 12, where the dashed line is an extrapolation from the single-point scatter using an exponent of  $-0.5$ , and the solid line is what we calculate

**Table 2**  
Observed Eclipse Spectra for CoRoT-2b. Values are in parts-per-million.

Wavelength (microns)	$\alpha$ Spectrum	Error	$\beta$ Spectrum	Error
1.125	334.6	67.4	248.6	86.0
1.169	272.4	83.7	366.7	109.6
1.218	339.4	119.3	309.0	83.2
1.278	344.2	72.0	313.5	60.5
1.324	338.9	64.7	279.9	56.8
1.369	403.9	77.1	376.2	60.1
1.424	454.5	59.8	480.9	65.5
1.475	320.3	93.5	304.8	80.3
1.525	438.3	62.6	454.6	63.4
1.574	548.7	61.3	632.1	61.9
1.619	382.2	82.2	414.0	73.8

from the actual data. These differential data are nearly photon-limited at almost all wavelengths, and  $\sigma(N)$  decreases very close to  $N^{-0.5}$ . We write  $\sigma(N) = a\sigma(1)N^b$  and we solve for  $a$  and  $b$ . We then use that relation to calculate the expected precision for the aggregate in-eclipse points and the aggregate out-of-eclipse points, and we propagate those errors to calculate the error on the differential eclipse depths.

As a check on the above error calculation, we also derive the precision of the differential eclipse directly using the residual-permutation method (Bouchy et al. 2005). Removing the best-fitting differential eclipse, we permute the residuals sequentially and add them back to the best-fit eclipse curve to make new data. Fitting to these re-cast data for all possible permutations (580 of them), we calculate the dispersion in the resultant differential eclipse depths. On average, we find that this produces excellent agreement with the first method described above. For our final spectrum and errors, we bin the results - and propagate the errors - to the same resolution (4 columns,  $0.05 \mu\text{m}$ ) that we used as a smoothing kernel in the wavelength jitter correction.

Figure 13 shows the exoplanetary spectrum from our analyses at single-column resolution (top panel, only  $\alpha$  results for illustrative purposes), and binned to a wavelength resolution of  $0.05 \mu\text{m}$  (bottom panel). The error bars on the  $\alpha$  binned spectrum in Figure 13 are 77 ppm on average, which is 25% greater than the photon noise. From our  $\beta$ -analysis, the binned spectrum is similar, and the errors average to 73 ppm (18% greater than the photon noise). The values of our binned spectra, and errors, are listed in Table 2.

## 7. IMPLICATIONS FOR THE ATMOSPHERE OF COROT-2B

No single model for the atmosphere of the planet fits all of the available data to within the errors. The observed properties of the planet's atmosphere include: 1) the optical eclipse observed by the *CoRoT* mission (Alonso et al. 2009; Snellen et al. 2010), 2) a ground-based eclipse near  $2 \mu\text{m}$  (Alonso et al. 2010), 3) the overall level, general slope with wavelength, and lack of obvious or known spectral features seen in our WFC3 data, and 4) eclipses in 3 Spitzer bands (Gillon et al. 2010; Deming et al. 2011). Figure 14 shows these data in comparison to several modeled spectra: a best-fit blackbody, conventional solar abundance models (Burrows et al. 2001; Burrows, Budaj, & Hubeny 2008; Burrows et al. 2008; Burrows et al. 2010), and a carbon-

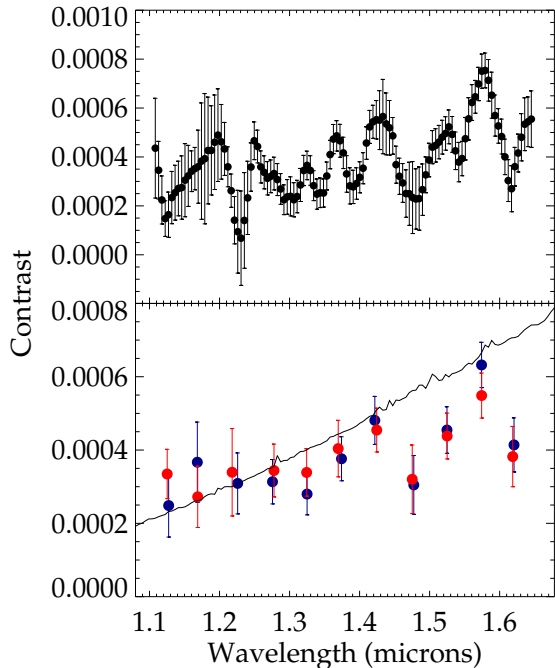


**Figure 13.** Top panel: Eclipse depth (as planet/star contrast) versus wavelength for the eclipse of CoRoT-2. Results from each detector column are plotted (from our  $\alpha$  analysis), so the smoothing used in the wavelength shift process creates the appearance of autocorrelation. Bottom panel: Spectra of CoRoT-2b from our  $\alpha$  (red points) and  $\beta$  analysis (blue points), binned to  $0.05 \mu\text{m}$  (4 column) resolution. The line is a 1788K blackbody for the planet.

rich model (Madhusudhan 2009; Madhusudhan & Seager 2010; Madhusudhan 2012). Although none of these are ideal fits to the data, each model has characteristics that account for some observed properties of the planet, as we now discuss.

### 7.1. A Blackbody Spectrum?

The lower panel of Figure 13 includes the contrast produced by a best-fit blackbody for the planet compared to the results from our  $\alpha$  and  $\beta$  analyses, and Figure 14 plots that blackbody in comparison to the totality of existing eclipse data. We adopt a Kurucz model for the star ( $T_{\text{eff}}=5750$ ,  $\log(g)=4.5$ ), yielding a best-fit blackbody temperature of  $1788 \pm 18\text{K}$  for the planet in our WFC3 band, from our  $\alpha$ -analysis. This blackbody temperature gives acceptable agreement with the infrared eclipse results at longer wavelength (Figure 14). The 1788K blackbody - derived from the WFC3 data alone - misses the ground+Spitzer eclipse amplitudes by an average of about  $1.8\sigma$ . However, a blackbody spectrum for the planet does not produce the best *slope* over the WFC3 band, as we now discuss.

Our observed WFC3 spectrum for CoRoT-2b has two striking features: 1) it slopes slightly upward with increasing wavelength, and 2) it shows little to no evidence for water absorption or emission in the  $1.4 \mu\text{m}$  band. Statistically, the first question to resolve is whether the simplest possible fitting function can account for our spectrum. The simplest function is a single value in contrast, i.e. a flat line at the average contrast level. For our  $\alpha$

analysis spectrum (red points on Figure 13) the  $\chi^2$  of the best-fit flat line is 12.8 for 10 degrees of freedom, so our  $\alpha$  analysis accepts a flat line as representing the planet's contrast across the WFC3 band. For our  $\beta$  analysis (blue points on Figure 12), the flat line  $\chi^2$  is 28.6, rejecting the flat line at  $> 99\%$  confidence. So our  $\beta$  analysis indicates a stronger and more significant upward slope than does our  $\alpha$  analysis. That is the single largest difference between our  $\alpha$  and  $\beta$  analyses, that are otherwise very consistent, with all points overlapping within their error bars (Figure 13). Both of our WFC3 analyses reject the best-fit blackbody slope for the planet, but only at about the 93% confidence level. The  $\chi^2$  values are 17.0 and 17.8 (10 degrees of freedom) for our  $\alpha$  and  $\beta$  spectra, respectively. On the other hand, the blackbody is obviously consistent with the weakness of water absorption in the WFC3 band.

We checked that our results are not affected by inadequate corrections for detector non-linearity at the high fluence levels of our data. We repeated the  $\beta$  analysis omitting the last (fourth) sample of the exposure, and using only the first 3 samples, where the fluence level ( $\sim 47,000$  electrons) is well within the linear regime. That modified version of the  $\beta$  analysis shows little difference from the  $\beta$  spectrum shown on Figs. 13 & 14 (but, with larger errors due to the lower fluence levels).

The slope of the planet's spectrum across the WFC3 band is relevant to the interpretation of the eclipse amplitude observed in the optical by CoRoT (Alonso et al. 2009; Snellen et al. 2010). If a 1788K blackbody agreed with the slope of our observed spectrum, it would be reasonable to extrapolate that blackbody to judge the magnitude of the thermal emission from the planet at optical wavelengths. A blackbody of 1788K would produce negligible thermal emission in the optical, and we would conclude that the optical eclipses are due to reflected light. However, given that the observed slope across the WFC3 band does not decline as strongly as a 1788K blackbody, it remains possible that the optical eclipses are due to thermal emission. That could happen, for example, if temperatures on the star-facing hemisphere of the planet were spatially inhomogeneous. Hotter regions having a small filling factor, combined with cooler regions of larger filling factor, could in principle produce the observed slope across the WFC3 band, and account for the optical eclipses, while still remaining consistent with the observed contrast at wavelengths exceeding  $2 \mu\text{m}$ .

In order to probe the viability of our speculation concerning temperature inhomogeneities, we performed exploratory fits (not illustrated) using two different blackbody temperatures and filling factors on the star-facing hemisphere of the planet. We find a good fit to our WFC3 and the CoRoT data using  $T_1 = 1500\text{K}$  and  $T_2 = 3600\text{K}$ , with filling factors of 0.96 and 0.04, respectively. This combination matches the level of the contrast in the CoRoT bands as well as the contrast level and wavelength dependence of our WFC3 results, but it significantly underestimates the contrast in the Spitzer bands (by about 0.001). Recent hydrodynamic simulations of hot Jupiter atmospheres show brightness temperature variations as large as a factor of two on the star-facing hemisphere of HD189733b (Dobbs-Dixon & Agol

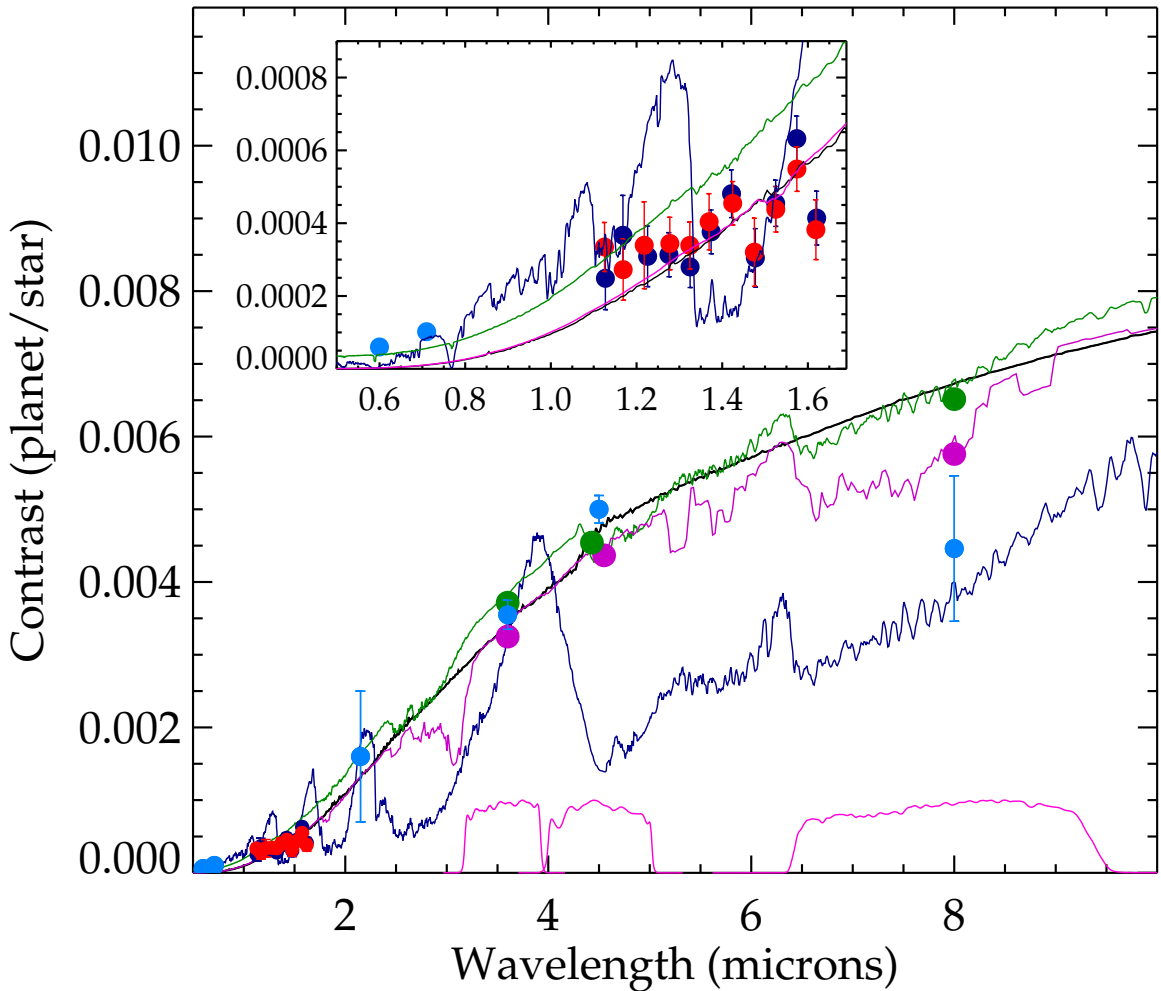


**Figure 14.** Our WFC3 results for CoRoT-2b shown in the context of ground-based  $2\mu\text{m}$  results (Alonso et al. 2010), the Spitzer results from Deming et al. (2011), and the optical eclipse depths from Alonso et al. (2009). The black line is an 1788K blackbody for the planet, and the dark blue line is a solar abundance clear atmosphere Burrows model previously used to interpret the Spitzer data (Deming et al. 2011). The green line is the solar abundance Burrows model with additional continuous opacity (see text). The magenta model is from Madhusudhan and has equal carbon and oxygen abundances. All of the models lack temperature inversions (see text). The inset shows our WFC3 results, from both our  $\alpha$  (red points) and  $\beta$  (blue) analyses. Note that the error in the overall level of the WFC3 points (Sec. 5.2) is much greater than the relative errors on individual points.

2013, submitted). Since that planet is less strongly irradiated than CoRoT-2, the temperatures found by our exploratory fits seem plausible. Nevertheless, we do not here attempt to model the atmosphere of CoRoT-2 using a self-consistent 3-dimensional approach (temperature varying with depth and with horizontal coordinate). Higher quality data, such as we anticipate from the James Webb Space Telescope, may justify such an approach in the future.

### 7.2. Limit on WFC3 Spectral Features

Both our  $\alpha$  and  $\beta$  spectra agree that a straight line (contrast increasing linearly with wavelength) gives a good account of our results across the WFC3 band: the  $\chi^2$  values for a linear fit (9 degrees of freedom) are 6.1 and 13.7 for our  $\alpha$  and  $\beta$  spectra, respectively. These values leave little room for absorption or emission by water vapor at  $1.4\mu\text{m}$ . In order to specify a limit on

the degree of water absorption or emission, we scale and fit a Burrows model to the data, using the model shown in blue on Figure 14. In order to make the limit responsive to the modulation caused by the actual water absorption (as opposed to the slope of the continuum), we allow for a linear baseline difference as a function of wavelength. We construct 10,000 trial data sets, adopting the error at each binned wavelength from our  $\beta$ -analysis, and we fit the model plus a linear baseline to each trial data set using linear regression. Based on the distribution of fitted amplitudes, we find an 85 ppm  $3\sigma$  limit on the amplitude of water absorption or emission, measured at the bandhead at  $1.38\mu\text{m}$ . This limit assumes that the shape of the water absorption is the same as in the Burrows model. The  $3\sigma$  limit of 85 ppm is significantly less than the already weak water absorption seen during transmission spectroscopy of the giant planets XO-1b and HD 209458b (Deming et al. 2013),

WASP-19 (Huitson et al. 2013; Mandell et al. 2013), and HAT-P-1b (Wakeford et al. 2013). This conclusion is significant, as can be seen by reference to one conventional solar abundance Burrows model (Burrows et al. 2001; Burrows, Budaj, & Hubeny 2008; Burrows et al. 2008; Burrows et al. 2010) illustrated as the dark blue line on Figure 14. This model is not intended as a fit to the WFC3 data, but it was invoked by Deming et al. (2011) in an attempt to account for the Spitzer observations. Although it misses the  $4.5\ \mu\text{m}$  Spitzer point, Deming et al. (2011) discussed the possibility of circumplanetary carbon monoxide emission in that band, due to tidal stripping by the star. However, this model produces a much larger spectral modulation in the WFC3 band than is seen in our observed spectra.

### 7.3. Solar Abundance Model Atmospheres

CoRoT-2b is an unusual planet, and the Spitzer data have been particularly difficult to understand, as discussed by Deming et al. (2011) (but, see Madhusudhan 2012). The relatively high contrast at  $3.6\text{-}4.5\ \mu\text{m}$  seems to require a hot continuum, allowing little if any molecular (principally water) absorption. Simultaneously, the lower contrast at  $8\ \mu\text{m}$  requires absorption to a significant degree. We here explore the potential for conventional solar abundance model planetary atmospheres to account for the totality of the CoRoT-2b eclipse data.

The weakness of absorption features can be produced in a solar abundance model by adding continuous opacity by small particle scattering and/or absorption. That could dampen features in the emergent spectrum at short wavelengths, but a reduced scattering cross-section with increasing wavelength could allow greater spectral contrast at  $8\ \mu\text{m}$  (mentioned by Deming et al. 2011). If the temperature remains nearly constant as a function of pressure/altitude in the planet’s atmosphere, that would also suppress any absorption or emission features in the emergent spectrum. Figure 14 shows the contrast from a Burrows model (Burrows et al. 2001; Burrows, Budaj, & Hubeny 2008; Burrows et al. 2010) having three additional sources of opacity not present in a clear atmosphere. This model is shown in green on Figure 14, and has redistribution parameter  $P_n = 0.1$  (Burrows, Budaj, & Hubeny 2008). The additional opacity sources are first, a high altitude optical ( $0.4\text{-}1.0\ \mu\text{m}$ ) absorber of opacity  $0.2\ \text{cm}^2\text{g}^{-1}$ . Second, an absorbing haze opacity of  $0.04\ \text{cm}^2\text{g}^{-1}$  uniformly distributed at all pressures and wavelengths, and third, a scattering opacity of  $0.08\ \text{cm}^2\text{g}^{-1}$  also uniformly distributed at all pressures and wavelengths. The scattering opacity acts to increase the reflected light, but not increasing the thermal emission. Note that in principle we could include a wavelength dependence to the opacity of the broadly distributed hazes, but we prefer to keep this *ad hoc* opacity as simple as possible.

The uniformly distributed hazes damp the spectral modulation in the WFC3 bandpass to an acceptable degree, but the model misses the overall WFC3 contrast level, being too high by 161 ppm. Like all single-spatial-component models, it’s slope across the WFC3 band is larger than our data. Given the error level of our white light eclipse ( $395^{+69}_{-45}$  ppm), the overall contrast difference is significant at  $2.3\sigma$ , which is the single largest problem

with this model. On the other hand, the scattering opacity increases the contrast in the optical to the point where it underestimates the *CoRoT* eclipse amplitude by less than  $2\sigma$ . Also, among the models we’ve tested, it does the best job of reproducing the long wavelength eclipse amplitudes ( $1.5\sigma$  on average).

The aggregate eclipse data are ambiguous concerning the possibility of a thermal inversion in the dayside atmosphere of CoRoT-2b. As discussed in Madhusudhan (2012), the lower brightness temperature in the  $8\ \mu\text{m}$  Spitzer bandpass compared to the brightness temperatures in the shorter wavelength channels (except  $4.5\ \mu\text{m}$ ) suggests a temperature profile decreasing outward in the atmosphere. If that gradient is flatter than radiative equilibrium models predict, it will help to account for the lack of strong spectral features. On the other hand, the solar abundance radiative equilibrium model (green line on Figure 14) achieves good agreement with the  $4.5\ \mu\text{m}$  Spitzer eclipse depth by incorporating  $0.2\ \text{cm}^2\text{g}^{-1}$  of extra optical-wavelength opacity at low pressures ( $\sim 1$  mbar) close to where radiation in the  $4.5\ \mu\text{m}$  band is formed (Burrows et al. 2007). Indeed, that model shows a temperature rise of about 75 Kelvins, near 0.2 mbars. But due to the more widely distributed absorbing haze, the temperatures in this model at high altitude are already hundreds of Kelvins over the values they would have in a clear atmosphere. To the extent that this model is preferred, or that a flattened temperature gradient counts as a weakly-inverted atmosphere, then CoRoT-2b could be claimed to have a temperature inversion. However, this evidence for an inversion is weaker than for HD 209458b (Burrows et al. 2007; Knutson et al. 2008), and is ambiguous in the sense that the atmosphere could be heated without satisfying a strict definition of inversion (temperature increasing with height). Knutson et al. (2010) hypothesized that planets orbiting active stars will not have strong atmospheric temperature inversions, because the absorbing species that causes the inversion (e.g., Hubeny et al. 2003; Fortney 2008) may be destroyed by the enhanced UV flux from stellar activity. CoRoT-2a is an active star (Guillot & Havel 2011), and lack of a strong thermal inversion in CoRoT-2b would support the Knutson et al. (2010) hypothesis.

### 7.4. A Carbon-rich Model Atmosphere

An alternate way to reduce the spectral modulation by water vapor in the WFC3 bandpass is to reduce the equilibrium water vapor mixing ratio, for example by increasing the carbon abundance relative to oxygen. This also helps to decrease absorption in the  $3.6\text{-}4.5\ \mu\text{m}$  bands (although methane does contribute some absorption at  $3.6\text{-}\mu\text{m}$ ), while preserving absorption at  $8\ \mu\text{m}$  via the  $7.8\ \mu\text{m}$  methane band. We used the methodology described by Madhusudhan (2009) and Madhusudhan & Seager (2010) to find a possible carbon-rich match to the aggregate data for this planet (except for the optical eclipses). Madhusudhan (2012) discussed CoRoT-2b and was able to fit the pre-WFC3 data by varying the C/O ratio to various degrees. The magenta line on Figure 14 is a model with an enhanced carbon abundance (C/O=1), and having a non-inverted atmosphere with modest thermal contrast (700K increase in temperature from upper boundary to the optically thick



photosphere). The enhanced carbon abundance weakens the water absorption, but allows sufficient absorption near  $8\mu\text{m}$  to account for that Spitzer point to within  $\sim 1\sigma$ . The average agreement with the ground+Spitzer eclipses is  $1.9\sigma$ , not quite as good as the blackbody and the solar abundance model. On the other hand, the carbon-rich model does the best job – of the atmospheric models, i.e., beyond just a linear fit – of reproducing the WFC3 spectrum ( $\chi^2 = 16.1$  for 10 DOF), and in particular it agrees essentially perfectly with the amplitude of the WFC3 white-light eclipse. It does not require additional haze opacity.

### 7.5. Reprise of the Model Atmosphere Comparisons

We here summarize the main conclusions from comparing the aggregate eclipse data for this planet with emergent spectra from different models. We tested a blackbody, as well as more sophisticated solar abundance and carbon-rich models. No model fits all of the data. The limit on spectral modulation due to water absorption in the WFC3 band is our main observational result. Given the lack of clear and unequivocal molecular absorption features in the WFC3 and other bands, emergent spectra more sophisticated than a blackbody are unproven. A blackbody spectrum gives an acceptable fit to the data except for the optical eclipses as seen by *CoRoT*. A blackbody spectrum fits the slope over the WFC3 band poorly, but multi-component blackbodies due to spatial inhomogeneities on the star-facing hemisphere have the potential to help account for the observations, including the optical eclipses as seen by *CoRoT*, especially if extra scattering opacity increases toward short wavelengths. Note that the absorbing and scattering hazes invoked in our solar abundance model are qualitatively similar to extra absorption and scattering opacity inferred for the archetype planet HD 189733b (Pont et al. 2013; Evans et al. 2013).

Although a blackbody spectrum reasonably accounts for the infrared eclipse data, it is not a model of the planet’s atmosphere *per se*. Instead, the planetary atmosphere can mimic a blackbody via the presence of extra continuous opacity that damps the observed thermal contrast, or due to a high carbon abundance that weakens the bands of the principal molecular absorber (water vapor). In either case, extra scattering opacity at optical wavelengths could help to account for the amplitude of the optical eclipses. We find only weak evidence for a strong temperature inversion, but extra absorbing opacity in the solar abundance model would perturb the temperature profile in a manner similar to a temperature inversion, but less extreme.

## 8. SUMMARY

We observed the Very Hot Jupiter CoRoT-2b in secondary eclipse using three visits by the WFC3 G141 grism on HST. Even without utilizing the new spatial scan mode, we obtained spectra with errors approaching the photon noise limit. We characterized the instrument-related systematic effects present in the data. We find a time-dependent variation in the background intensity, a visit-long slope, slopes associated with each orbit, and we investigate the ‘hook’ effect that occurs after data transfers. We explored the behavior, dependencies, and how best to account for these effects in data analyses. In

particular, we defined the amplitude of the hook effect versus the exposure level in electrons (Figure 6).

We measure the thermal emission from the planet in the 1.1-1.7  $\mu\text{m}$  band, but we find no spectral features to a  $3\sigma$  limit of 85 ppm. We used a differential method to derive the spectrum and cancel the systematic errors (Deming et al. 2013), obtaining results close to photon-limited. No model fits all available eclipse data for this planet to within the errors. We consider solar abundance and carbon-rich spectral models, as well as a simple blackbody spectrum, to account for the eclipse data. The spectral models do not clearly surpass the blackbody spectrum in terms of the quality of the fit. The slope of the data within the WFC3 bandpass is less than given by all of the models, including the best-fit blackbody. There is weak and ambiguous evidence that the atmospheric temperature structure is inverted, but a reduced temperature gradient may be present, and may help to mimic the quasi-blackbody nature of the emergent spectrum. Extra atmospheric continuous opacity is a strong possibility to account for the lack of spectral features in the WFC3 band. If that opacity has a scattering component, it can help to account for the optical eclipse amplitude of this planet as observed by *CoRoT*. Spatial inhomogeneities in temperature on the star-facing hemisphere may also help to account for the optical eclipse and the slope of the spectrum in the WFC3 band.

## REFERENCES

- Alonso, R., Deeg, H. J., Kabath, P., & Rabus, M. 2010, *AJ*, 139, 1481
- Alonso, R., Guillot, T., Mazeh, T., et al. 2009, *A&A*, 501, L23
- Alonso, R., Auvergne, M., Baglin, A., et al. 2008, *A&A*, 482, L21
- Berta, Z. K., Charbonneau, D., Désert, J.-M., et al. 2012, *ApJ*, 747, 35
- Bouchy, F., Pont, F., Melo, C., Santos, N. C., Mayor, M., Queloz, D., & Udry, S. 2005, *A&A*431, 1105
- Burrows, A., Hubbard, W. B., Lunine, J. I., & Liebert, J., 2001, *Rev.Mod.Phys.* 73, 719.
- Burrows, A., Hubeny, I., Budaj, J., Knutson H. A., & Charbonneau, D., 2007, *ApJ*, 668, L171
- Burrows, A., Budaj, J., & Hubeny, I., 2008, *ApJ*, 678, 1436.
- Burrows, A., Ibgui, L., & Hubeny, I. 2008, *ApJ*, 682, 1277
- Burrows, A., Rauscher, E., Spiegel, D. S., & Menou, K., 2010, *ApJ*, 719, 341.
- Crouzet, N., McCullough P. R., Burke, C., & Long, D., 2012, *ApJ*, 761, id.7.
- Deming, D., Knutson, H., Agol, E., et al. 2011, *ApJ*, 726, 95
- Deming, D., Wilkins, A. N., and 19 co-authors 2013, *ApJ*, 774, id.95.
- Dobbs-Dixon, I., & Agol, E. 2013, submitted to *MNRAS*, astro-ph/1211.1709.
- Evans, T. M., & 9 co-authors, 2013, *ApJ*, 772, id.L16.
- Fortney, J. J., Lodders, K., Marley, M. S. & Freedman, R. S. 2008, *ApJ*, 678, 1419
- Gibson, N. P., Pont, F., & Aigrain, S. 2011, *MNRAS*, 411, 2199
- Gillon, M., Demory, B.-O., Barman, T., Bonfils, X., Mazeh, T., Pont, F., Udry, S., Mayor, M. & Queloz, D., 2007, *A&A*471, L51
- Gillon, M., Lanotte, A. A., Barman, T., et al. 2010, *A&A*, 511, A3
- Guillot, T., & Havel, M. 2011, *A&A*, 527, A20
- Hubeny, I., Burrows, A., & Sudarsky, D. 2003, *ApJ*, 594, 1011
- Huitson, C. M., & 16 co-authors, 2013, *MNRAS*, 434, 3252.
- Knutson, H. A., Charbonneau, D., Allen, L. E., Burrows, A., & Megeath, S. T., 2008, *ApJ*, 673, 526.
- Knutson, H. A., Howard, A. W., & Isaacson, H. 2010, *ApJ*, 720, 1569
- Kümmel, M., Walsh, J. R., Kuntschner, H., & H., B. 2011, *aXe User Manual*, 2nd edn.

- Kuntschner, H., Bushouse, H., Kümmel, M., & Walsh, J. R. 2009, WFC3 SMOV Proposal 11552: Calibration of the G141 Grism, Tech. Rep. WFC3-209-17, Space Telescope - European Coordinating Facility
- Lanza, A. F., Pagano, I., Leto, G., et al. 2009, *A&A*, 493, 193
- Line, M. R., Knutson, H., Deming, D., Wilkins, A., & Desert, J.-M., 2013, *ApJ*, .
- Madhusudhan, N. & Seager, S. 2009, *ApJ*, 707, 24
- Madhusudhan, N., & Seager, S. 2010, *ApJ*, 725, 261
- Madhusudhan, N. 2012, *ApJ*, 758, 1
- Mandel, K., & Agol, E. 2002, *ApJ*, 580, L171
- Mandell, A., Haynes, K., Sinukoff, E., Madhusudhan, N., Burrows, A., & Deming, D., 2013, *ApJ*,
- McCullough, P. M., & MacKenty, J., 2012, Instrument Science Report WFC3 2012-08, Baltimore: Space Telescope Science Institute.
- Pont, F., Sing D. K., Gibson N. P., Aigrain S., Henry, G., & Husnoo, N., 2013, *MNRAS*, 432, 2917.
- Ranjan, S., Charbonneau, D., Desert, J-M, Madhusudhan, N., Deming, D., Wilkins, A. N., Burrows, A., & Mandell, A. 2013 Submitted to *ApJ*
- Rajan, A. 2010, WFC3 Data Handbook, STScI, Baltimore, MD
- Sada, P. V., and 10 co-authors, 2012, *PASP*, 124, 212.
- Schröter, S., Czesla, S., Wolter, U., et al. 2011, *A&A*, 532, A3
- Smith, R. M., Zavodny, M., Rahmer, G., & Bonati, M. 2008, *Proc. of the SPIE* 7021, 23
- Snellen, I. A. G., de Mooij, E. J.W., & Burrows, A. 2010, *A&A*, 513, A76
- Swain, M., & 9 co-authors, 2013, *Icarus*, 225, 432.
- Wakeford, H. R., & 15 co-authors, 2013, *MNRAS*, in press.